Determination of Macroscopic Optical Properties of Multilayer Random Media by Remote Sensing

Randall L. Barbour, Harry L. Graber, Raphael Aronson*, and Jack Lubowsky

Depts. of Pathology and Biophysics, SUNY Health Science Center at Brooklyn, 450 Clarkson Ave., Brooklyn, NY 11203, *Dept. of Physics, Polytechnic University, 333 Jay St., Brooklyn, NY 11201

Abstract

Several measurement and analysis schemes have been explored, using simulated data, in an effort to identify new strategies for the determination of the macroscopic optical properties of multilayer random media. Several simple algorithms are described which are capable of identifying the values of important parameters such as the total cross-section, Σt, the ratio of the absorption to total-cross section, $\Sigma a/\Sigma t$, and depth of subsurface boundaries in two- and three-layer media. The albedo values of the media varied from 0.9 to 0.99 and the superficial layer had an absorptivity either greater or less than the subsurface layers. A novel feature of the algorithms is a comparison of the responses of coupled pairs of detectors. Their utility stems from the fact that variations in the orientation and location of collimated detectors permit the selective interrogation of subsurface regions in dense scattering media

1. Introduction

In many studies involving dense scattering media, a remote sensing measurement affords the only practical means to interrogate the medium of interest. These studies typically seek to identify the depth at which a boundary may exist, and the absorption and scattering properties of the various layers. For optical studies of tissue, characterization of such parameters has special relevance to many applications in clinical medicine, especially if they are obtainable from a backscatter measurement. In recent years several groups have described algorithms, derived from diffusion theory, which attempt to characterize the properties of two-layer media by analyzing the intensity of measured (or calculated) diffusely backscattered light[1-6]. For the most part, these studies have had only limited success. For example, Taitelbaum *et al.*[5] concluded that whereas it was possible to detect the presence of a second layer having less absorption than the top layer, detection of the reverse case was not possible. Moreover, even in the former case, signal-to-noise considerations would limit detection of the second layer to depths close to the surface ($\leq$3 mean free paths (MFP)). More recently, Schmitt *et al.*[6] have derived solutions to the diffusion equation which enable them to predict the distance dependence of the intensity of diffusely backscattered light for a two-layer medium provided the optical properties of the two layers are known. The more important task, however, is to solve the inverse problem; *i.e.*, to deduce the optical properties given only the intensity of backscattered light.

As with any measurement scheme, the ability to detect a change in the properties of a medium must lie in obtaining a differential detector response to the presence of a temporal or spatial discontinuity. Although this observation is somewhat obvious, the way to develop a measurement scheme which would respond optimally to changes in the optical properties within a region of a diffusing medium, or to changes in the location of a boundary between regions, has not been obvious. Recently, we have demonstrated that the ability to preferentially probe a random medium is strongly dependent on the position and orientation of the receiver and its degree of collimation, even in the limit of isotropic scattering[7,8]. We have also shown that knowledge of this relationship can be used as the basis for deriving an image reconstruction algorithm[9-13]. In this report we have extended our previous studies,

 0-8194-0521-3/91/$4.00

and have explored various measurement and analysis strategies which implicitly recognize the above dependence and apply them to evaluating multilayer media.

2. Methods

2.1 Monte Carlo Methods

All media modeled had infinite length and width, depth was either finite or semi-infinite. All medium surfaces and/or layer boundaries were planar, the layer boundaries within a medium were parallel to each other and to the surface. Photons entered the medium at a single point, normal to the surface. The one-dimensional nature of the heterogeneity meant that the surface emission profile was always radially symmetric; then the detected intensity, I, is a function only of the source-detector separation, R, and the inclination, Θ, and azimuthal, Φ, angles of the detector, as shown in Figure 1 below.

Figure 1

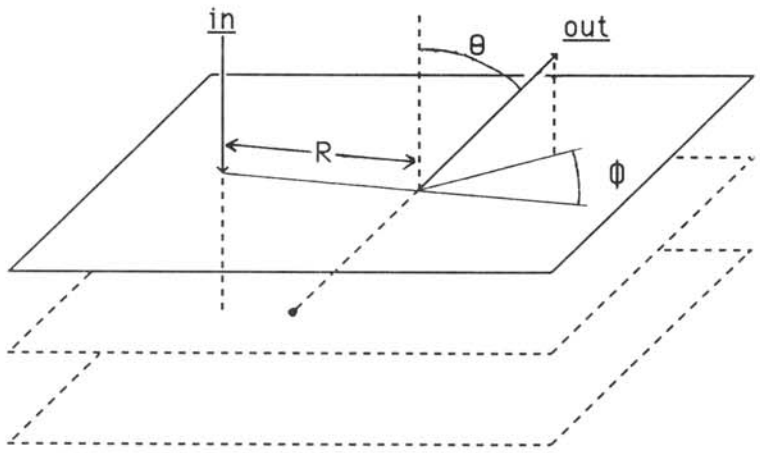

Each detector ring recorded all emerging photon scores within a certain range of distances (R, R+ΔR) from the point of injection. In some cases ΔR was 1.0 MFP for all detectors; in others ΔR was 0.25 for R$\leq$10 and 0.5 for R>10. All scores within a single distance bin were sectioned among 12 "solid angle sectors", SAS, according to the direction of the scoring photon's final flight segment in the medium. Each SAS subtends 30° in Θ and 90° in Φ.

In the simulations of surface emission profile measurements, the quantities scored were detected intensity (in photons detected/ incident photon/ MFP^2/ sr), number of collisions, n, total distance traveled in the medium, d, and maximum propagation depth, Z. Average values of the latter three were subsequently calculated for each detector. Weight functions were calculated, as described previously[12] , by multiplying, in each volume element, the average collision density when photons entered the medium from the source, and the corresponding average collision density for photons launched along the axis of the detector (*i.e.,* adjoint intensity). It should be noted that unlike the rather large acceptance angles of the collimated detectors used in the calculation of the surface emission profiles, point-collimated detectors were used for calculation of weight functions. A detailed description of the scoring functions used, of the equations used to determine the intercollision distance and post-scattering direction, of techniques used to maximize the efficiency of the calculation (modeling photon ensembles, renormalization, Russian roulette, correlated sampling) and calculation of the weight functions has been reported elsewhere[12].

2.2 Calculation of Surface Emission Profile by Diffusion Approximation

The light intensity recorded by an uncollimated cosine detector is equal to the vertical component of the gradient of diffuse photon density Φ, which was in turn calculated using the integral equation form of the diffusion equation[14].

$$\Phi(\mathbf{r}) = \int_V S(\mathbf{r}')G(\mathbf{r}, \mathbf{r}')dV' \tag{1}$$

$$I(R) = D\,[\partial\Phi(R)/\partial z]_{z=0} \tag{2}$$

The source distribution function, $S(\mathbf{r})$, for a point-collimated source normally incident on a half-space medium, is:

$$S(\mathbf{r}) = \Sigma s \exp(-\Sigma_t z)\delta(R) \tag{3}$$

where, Σs = macroscopic scattering cross-section, cm^{-1}; Σt = macroscopic total collision cross-section, cm^{-1}; $\delta(R)$ = Dirac delta function.

The diffusion kernel, $G(\mathbf{r}, \mathbf{r}')$, for a homogeneous half-space medium was calculated by the method of images[14]. When the diffusion kernel and source function are substituted into eq. 1, eq. 2 becomes:

$$\begin{aligned} I(R) = \Sigma s/4\pi \int_0^\infty \exp(-\Sigma_t z')[z'(1 + k(R^2 + z'^2)^{1/2})(R^2 + z'^2)^{-3/2} \exp(-k(R^2 + z')^{1/2}) \\ + (z' + 2z_o)(1 + k(R^2 + (z' + 2z_o)^2)^{1/2})(R^2 + (z' + 2z_o)^2)^{-3/2} * \\ \exp(-k(R^2 + (z' + 2z_o)^2)^{1/2})]\, dz' \end{aligned} \tag{4}$$

where, $z_o = .71/\Sigma t$ = extrapolation distance, cm; $k = \sqrt{(\Sigma a/D)}$ = reciprocal of diffusion length, cm^{-1}; Σa = macroscopic absorption cross-section, cm^{-1}; D = diffusion constant, cm. The integral in equation 4 was evaluated numerically, by a combination of the composite Gauss quadrature and Laguerre quadrature algorithms[15].

3. Results

When attempting to deduce the properties of a multilayer random medium, often the only information available is the intensity of diffusely backscattered light. Figure 2 is a plot of the surface emission profile from nonabsorbing homogeneous, partially absorbing homogeneous, and partially absorbing three-layer media. The curve corresponding to the layered medium is remarkable only for its qualitative similarity to those for the homogeneous media. While the transitions between the layers occur at sharp, well-defined boundaries, there are no discontinuities or other features apparent in the plot that reveal the presence of heterogeneity in the medium. Conversely, there is no simple way of reading the value of $\Sigma a/\Sigma t$ directly off the plot of logI vs. R even for the homogeneous media. Results in Figure 3 demonstrate that in the case of a half-space medium with isotropic scattering, the value of $\Sigma a/\Sigma t$ can be readily determined by constructing a plot of logI/logIo vs. R. At distances greater than 4-5 MFP from the source this ratio is strictly linear with R at all values of absorption examined ($\Sigma a/\Sigma t$ = .01-.10 for Monte Carlo data and for data calculated using equation 4, the diffusion approximation), and demonstrates that a simple relationship of I = Io **(aR+b) holds, where a is proportional to $\sqrt{(\Sigma a/\Sigma t)}$, (see inset of Figure 3). Inspection of this Figure thus shows that if either

the MFP or the absorption probability is known, the other can be obtained directly from a plot of logI/logIo vs. R.

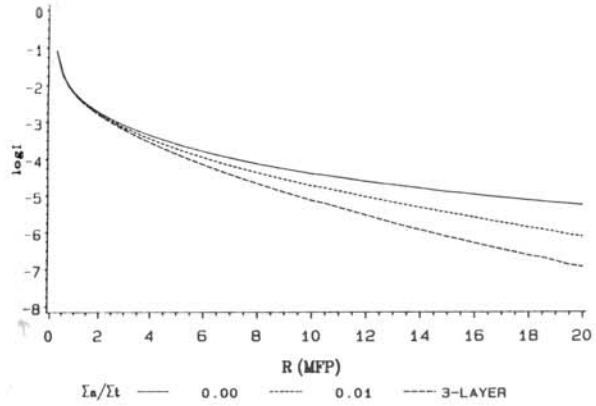

Figure 2. Plot of intensity, I, of backscattered photons versus distance separating source and detector, R. Results shown were obtained by Monte Carlo simulations as described in Methods for uncollimated detectors. Composition of the three-layer medium was: Top layer, $\Sigma a/\Sigma t = 0.01$, thickness = 2 MFP; middle layer, $\Sigma a/\Sigma t = 0.05$, thickness = 4 MFP; bottom layer, $\Sigma a/\Sigma t = 0.01$, thickness = ∞.

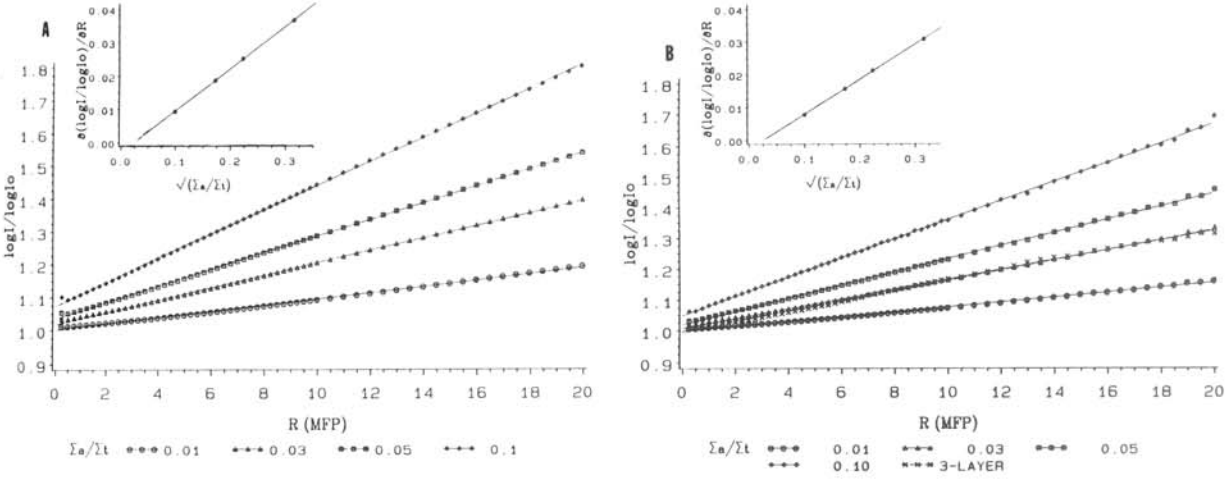

Figure 3: Abscissa: Distance separating source and detector, R, in MFP. Ordinate: Ratio of log of intensity, I, for homogeneous medium with non-zero $\Sigma a/\Sigma t$, to log of intensity, Io, for nonabsorbing homogeneous medium. Inset: replot of slopes of logI/logIo vs. R, plotted against $\sqrt{(\Sigma a/\Sigma t)}$. Panel A, data calculated from solution of diffusion equation (see equation 4 in Methods) for homogeneous half-space media; Panel B, data calculated from Monte Carlo simulations with homogeneous half-space media. Lines drawn were calculated by linear regression and correspond to media having the indicated values of $\Sigma a/\Sigma t$. Composition of the three-layer medium is the same as described in the legend of Figure 2.

When plots of logI/logIo vs. R were prepared for homogeneous slabs of finite thickness (≤32 MFP), nonlinear curves were obtained (data not shown). This suggested that a plot of this type may be useful in identifying the location of a boundary, as a medium having finite thickness is equivalent to a two-layer medium with a very large absorption cross-section in the second layer. However, when the data from the three-layer medium shown in Figure 2 were plotted in the same manner, no significant departure from the linear behavior was observed (see Figure 3B). Evidently, for this relationship, departure from linearity requires a large change in either the absorption or total cross-section across the boundary.

A careful study was made of the dependence of the shape of logI/logIo vs. R on the orientation of collimated detectors. This was examined because we had previously shown that the varying the detector orientation at a fixed R will result in the detector probing different portions of the medium. An illustration of this is shown in Figure 4. The average value of the greatest depth attained by the detected photons, <Z>, depends on Θ, the detector axis angle of inclination to the surface; it also varies (not shown) with Φ), the azimuthal angle of the detector axis. This dependence is present at all values of R (Figure 4A) and all values of $\Sigma a/\Sigma t$ (Figure 4B) studied.

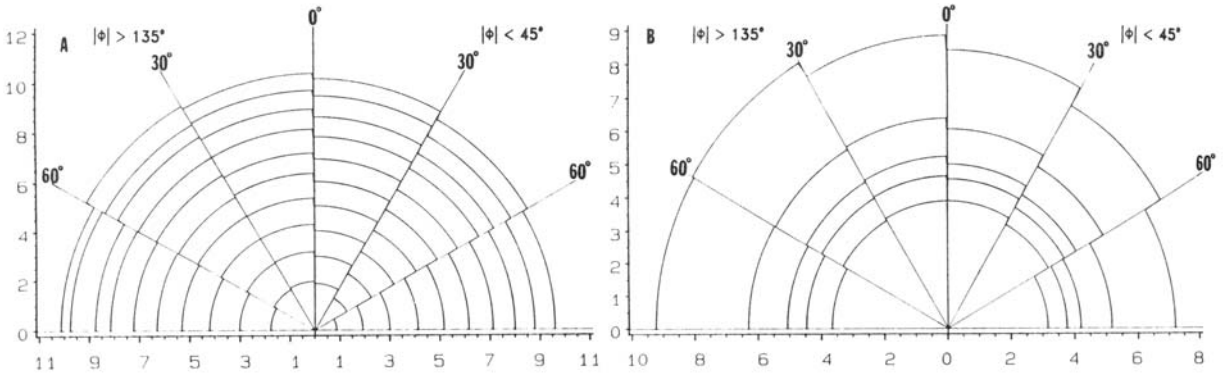

Figure 4: Plots, in polar coordinates, of the average value of the maximum depth reached in the medium by the detected photons, <Z>, as a function of angle of inclination, Θ, of collimated detector axis. Panel A, $\Sigma a/\Sigma t$ is fixed at .01, each curve shows results for detectors at different R, from 2-20 MFP in 2 MFP steps. Panel B, R is fixed at 10 MFP, each curve results for medium with different value of $\Sigma a/\Sigma t$. The five curves included on the graph are for $\Sigma a/\Sigma t$ = 0, .01, .03, .05, and .01. Collimated detectors are the solid angle sectors referred to in Methods; each subtends 30° in Θ and 90° in Φ.

The results shown in Figure 4, and analogous results (not shown) for <n>, average number of collisions, and <d>, average distance traveled, indicate that variations in detected intensity with orientation can be related to variations in the portions of the medium preferentially probed by the detected light. It was of interest, then, to see if the effect of homogeneous absorption on detected intensity varies among the different SAS. When intensity data for an individual SAS were plotted in the manner of Figure 3, it was found that in many cases logI/logIo vs. R was linear, although the proportionality constant relating the slope to $\sqrt{(\Sigma a/\Sigma t)}$ was different than that obtained for uncollimated detectors, and from one SAS to the next.

Whether logI/logIo is linear with R or not, it can be seen that if $\Sigma a/\Sigma t$ is plotted as a third axis in Figure 3, the family of lines for a given detector configuration would define a surface. Such a surface is conveniently displayed as a contour map, as in Figure 5A. As indicated above, surfaces for any two SAS would be different. This means that Σt and $\Sigma a/\Sigma t$ could be determined simultaneously for a homogeneous medium, as shown in Figure 5B and 5C. In principle, this requires as few as two measurements of diffuse reflectance with collimated detectors. A single measurement at a distance of R' physical units from the point of illumination is consistent with pairs of values of R, in MFP, and $\Sigma a/\Sigma t$ lying on a single contour of the surface for that particular detector configuration. Another measurement at the same R' but different detector orientation likewise corresponds to a single contour of another such surface. These two will have a unique intersection, which determines the $\Sigma a/\Sigma t$ of the medium and the number of MFP in the physical distance R'.

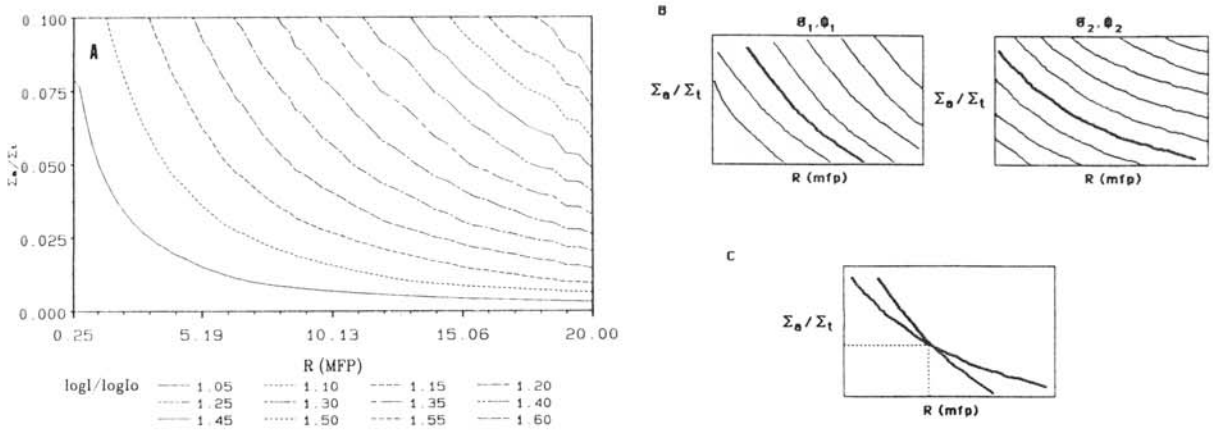

Figure 5: Panel A. Contour representation of the surface obtained, for a detector configuration, by plotting logI/logIo vs. R vs. $\Sigma a/\Sigma t$. If logI/logIo is linear in R, with slope $\sim \sqrt{(\Sigma a/\Sigma t)}$, then each contour has the functional form $(\Sigma a/\Sigma t) = k/R^2$. Panel B. A single measurement of diffusely reflected light is consistent with all points along a single contour on the surface for detectors of that configuration. Panel C. Two contours, each corresponding to a measurement at the same physical distance R' but different detector orientations, intersect at a single point. This gives the only value of R and $\Sigma a/\Sigma t$ consistent with both measurements.

The observation that the average depth of detected photons is sensitive to detector orientation and position (Figure 4) suggests that this algorithm may prove useful in examining stratified media. Data shown in Figure 6 are results of applying the algorithm to Monte Carlo data from six different media. One was homogeneous and served as control. Three others had two layers, to test the effects of reversing thc contrast between the layers and of varying the thickness of a less absorbing surface layer over a more heavily pigmented lower layer. The remaining two were three-layer "sandwiches" with the same value of $\Sigma a/\Sigma t$ in the first and third layer.

The graph of apparent (calculated) $\Sigma a/\Sigma t$ vs. R in Figure 6A shows that each of the three medium types yields a curve with a characteristic shape. As expected, the homogeneous medium gives estimates of $\Sigma a/\Sigma t$ very close to the true value at all values of R. Results from analysis of the two-layer media give apparent values of $\Sigma a/\Sigma t$ near that of the top layer for small R, but as R increases the calculated value of $\Sigma a/\Sigma t$ approaches the true value for the second layer. The rate at which it approaches the second-layer value decreases as the thickness of the first layer increases. For the three-layer media, the apparent value of $\Sigma a/\Sigma t$ is close to the true value of the first layer for small R, approaches the value of $\Sigma a/\Sigma t$ for the second layer as R increases and then reverses direction and approaches the value for the third layer at still larger R. Here, too, the rates of these deviations decrease as the second-layer thickness increases.

Calculation of the apparent MFP for one- and two-layer media is shown in Figure 6B. The control medium gives values of the apparent MFP close to the true value for all R. For the two-layer media, the calculated MFP is always underestimated when the superficial layer is more dark, and always overestimated when this layer is less dark, than the second layer. This behavior can be accounted for by the following. Results shown in Figure 4 and previous studies[7,12,16] show that photons entering

distant detectors have spent most of their time at depths far below the surface. Thus, the absorption properties of the second layer will largely determine the rate at which I falls with increasing R. As photons emerge from the second layer and propagate to the detector, they travel through a superficial layer which absorbs either more or fewer photons per unit distance than does the deeper layer. Thus, the detector will see less or more light, respectively, than it would had the entire medium had the same optical properties as the second layer. The effect of this will make the detector "behave" as if it were farther from or closer to, respectively, the point of illumination than it actually is.

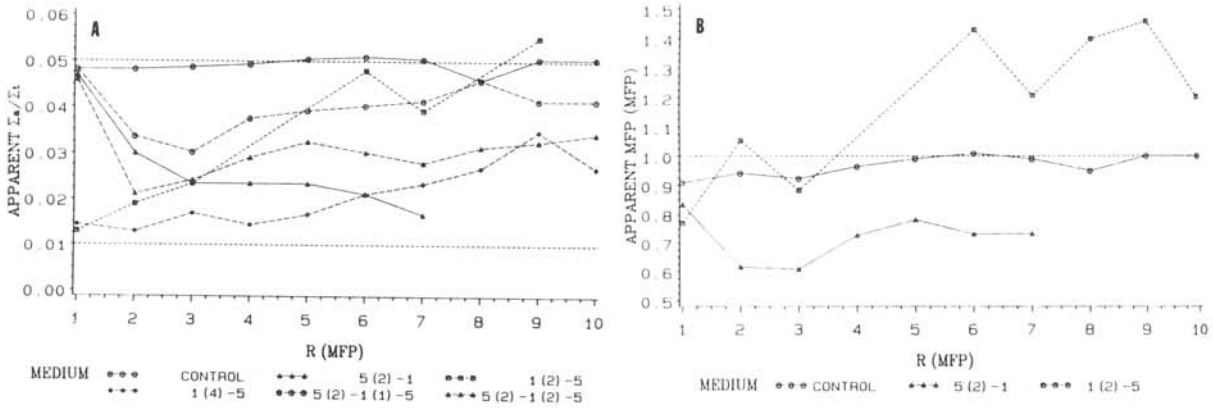

Figure 6: Result of applying algorithm of Figure 5 to surface intensity profiles calculated, as described in Methods, for media with 1, 2, or 3 layers. Detector configurations used in calculation of $\Sigma a/\Sigma t$ and MFP were Θ = 0-30°, $|\Phi|$ = 135-180°, and Θ = 60-90°, $|\Phi|$ = 0-45°. Medium 1 (○—○) (control): homogeneous, $\Sigma a/\Sigma t$ = .05, thickness = ∞; Medium 2 (△—△): two layers; top layer, $\Sigma a/\Sigma t$ (thickness (MFP)) = .05(2), bottom layer = .01 (∞); Medium 3 (□···□): two layers; top layer = .01(2), bottom layer = .05(∞); Medium 4 (◇-·-◇): two layers; top layer = .01(4), bottom layer = .05(∞); Medium 5 (○-·-○): three layers; first layer = .05(2), second layer = .01(1), third layer = .05(∞); Medium 6 (△-·-△): three layers; first layer = .05(2), second layer = .01(2), third layer = .05(∞). Panel A, apparent value of $\Sigma a/\Sigma t$, Panel B, apparent value of MFP.

Careful inspection of Figure 6 shows that several data points are missing from the plots, in particular at R = 4 or 5. The reason for this is that the two relevant contours did not intersect. That is, there is no homogeneous medium that would give the same result as this particular two-layer medium, at these distances and detector orientations. This result establishes that the medium must be stratified, but does not yield any information about its structure. In addition to this limitation, practical implementation of this algorithm would either require tabulation of a large amount of logI/logIo data from various homogeneous media or necessitate a significant amount of interpolation between known values of logI/logIo.

The tendency for apparent $\Sigma a/\Sigma t$ values to resemble the true value for the superficial layer at small R and to approach that of deeper layers as R increases is wholly consistent with the result shown in Figure 4. In earlier work[12,17], we showed that the portion of the medium probed by the light detected for a given source-detector configuration can be quantitatively described by a "weight function". The weight at a point in the medium is proportional to the light intensity at that point due to the illumination of the medium, and to the adjoint intensity at the detector (*i.e.*, the light intensity at the detector if a unit source were placed in the medium at the point of interest). Clearly, the relative

contribution of a region to the total weight determines the smallest departure from the optical properties of the surrounding medium that a given source-detector pair could recognize. If the goal is to detect the boundary between two layers with disparate properties, then a promising strategy would be to conduct a series of measurements (*e.g.*, sweeping a detector through a range of Θ at a fixed R) in which a region contributing a significant fraction of the total weight lies first on one side of the boundary, then straddles it, and then lies on the other side. An "optimal analysis algorithm" to accompany this "optimal measurement scheme" would use as input a comparison of measurements among two or more detector readings, rather than treating them separately.

An illustration of such a measurement scheme, and its effectiveness in locating a boundary, is shown in Figure 7. Contrast ratios such as these reveal the degree of differential detector response of a pair of detectors for the depths which straddle a layer boundary. If the contrast ratio has a value much different from 1.0, then a change in optical properties on only one side of the boundary will have a much greater impact on the intensity of light received by one of the detectors than on the other. More important is the shape of the curves in Figure 7, which indicate that as a distance scan is performed with a pair of coupled detectors, they will proceed from an initial state in which both receive a greater contribution to their total weight from the region above the boundary, to a point of maximum contrast at which only the far detector receives a greater contribution from the region below the boundary to a state in which both have the larger contribution coming from below the boundary. The depth of the boundary should be deducible from knowledge of R_{near}, ΔR, and the detector orientations.

The measurement scheme and analysis strategy suggested by this result is to record the intensity detected by families of pairs of detectors with fixed separation and/or orientation; calculate the ratio $\log I_{far}/\log I_{near}$ (or $\log I_{\Theta 1}/\log I_{\Theta 2}$, for the case of colocated detectors with different orientations), then compare this to the corresponding ratio for a homogeneous reference medium having the same optical properties as the superficial, physically accessible, layer. The result of this calculation would be exactly 1.0 if the medium being probed were also homogeneous. If it is stratified, however, the result should be near 1.0 for small R_{near}, and deviate as R_{near} increases.

Whether the "double ratio" increases or decreases as R_{near} increases would depend on whether $\Sigma a/\Sigma t$ in the second layer is greater or less than that in the first. The value of R_{near} at which significant deviation from 1.0 begins should increase as the thickness of the first layer increases, and the greatest (lowest) value reached and the derivative in the rising (falling) portion of the curve should depend on the ratio of Σa's in the two layers.

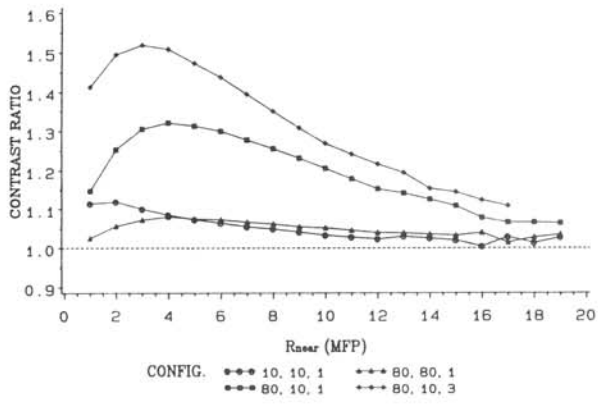

Figure 7. Contrast ratio for four families of detector pairs calculated at boundary between first and second layer (z=3), for a three layer medium, plotted against R. Composition of medium: first layer, $\Sigma a/\Sigma t$ (thickness (MFP)), = .01(3), second layer = .05(4), third layer = .01(∞). Constrast is defined as $w(z_b\text{-}1, z_b)/w(z_b, z_b+1)$, where w(z, z+1) is the contribution of the layer berween z and z+1 to the total weight for a source-detector pair, and z_b is the depth at which a boundary is present. Configuration of point-collimated detector pairs: (O—O), both detectors inclined 10° from normal,

ΔR = 1 MFP; (Δ—Δ), both detectors inclined 80° from normal, ΔR = 1 MFP; (□—□), near detector inclined 80° from normal, far detector 10°, ΔR = 1 MFP; (◇—◇), same as in 3 except ΔR = 3 MFP.

All of these expectations are borne out in the results shown in Figure 8. Panels A and B show the result when $(\log I_{far}/\log I_{near})(\log I_{near}/\log I_{far})_{ref}$ is calculated for two-layer media in which the thickness and $\Sigma a/\Sigma t$ of the first layer are held constant and $\Sigma a/\Sigma t$ of the second layer is varied. In these examples, the initial segments of the plots are nearly linear, and the value of R_{near} at which best-fitting lines intersect horizontal lines drawn at the level of peak displacement is independent of the ratio of Σa's in the two layers. This is an important observation, as it directly suggests a means to identify the depth of a boundary. Panels C and D show a similar plot for two-layer media in which $\Sigma a/\Sigma t$ is fixed in both layers and the thickness of the first layer is varied. In these examples, the value of R_{near} at which, lines tangent to the points where the absolute value of the slope is greatest intersect horizontal lines at the level of greatest displacement from 1.0, increases linearly with increasing thickness of the first layer. Panels E and F show the corresponding plot for three-layer media in which $\Sigma a/\Sigma t$ is fixed in all three layers, the thickness of the first layer is fixed and the thickness of the second layer is varied. It is seen in these examples that the presence of a third layer produces an appearance of a plot distinctly different from that for the two-layer case, drastically reducing the range of R in which the double ratio maintains its maximum displacement from 1.0. It is also apparent from these plots that the effects of the two interlayer boundaries are separable if ΔR is greater than the interboundary distance. However, if the second layer is thin, the second and third layers both influence the value of the double ratio from the outset. This feature may be useful in determining the thickness of subterranean layers.

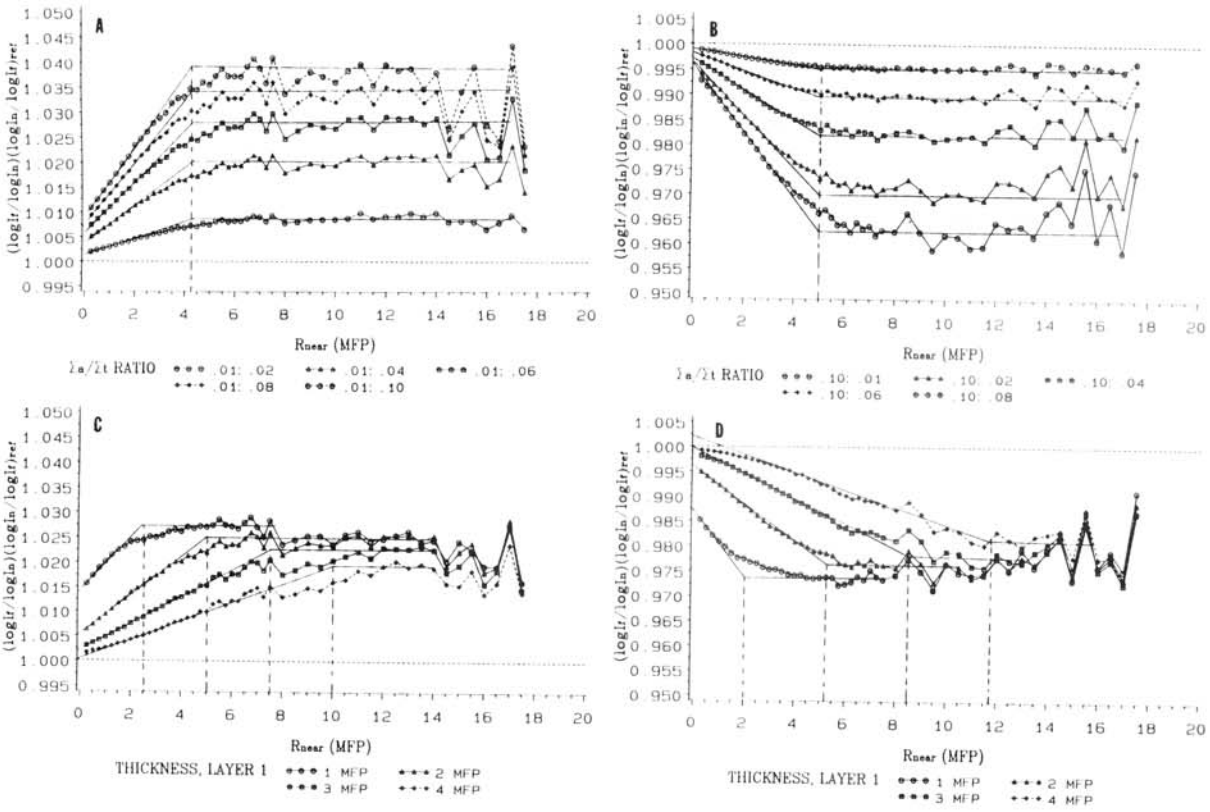

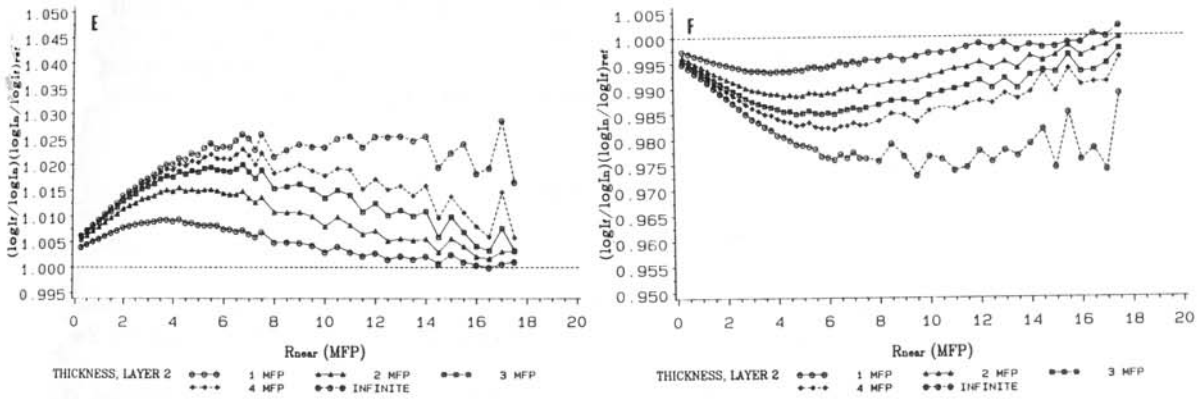

Figure 8. Plots of $(\log I_{far}/\log I_{near})(\log I_{near}/\log I_{far})$ref vs. R for two- and three-layer media. The reference medium is a homogeneous half-space with the same $\Sigma a/\Sigma t$ and Σt as the first layer of the stratified media. Panel A: two-layer media; first layer $\Sigma a/\Sigma t$ (thickness(MFP)) = .01(2); second layer = .02 to .10(∞). Panel B: two-layer media; first layer = .10(2); second layer = .01 to .08(∞). Panel C: two-layer media; first layer = .01(1-4); second layer = .05(∞). Panel D: two-layer media; first layer = .05(1-4); second layer = .01(∞). Panel E: three-layer media and two-layer limiting case; first layer = .01(2); second layer = .05(1-4, ∞); third layer = .01(∞). Panel F: three-layer media and two-layer limiting case; first layer = .05(2); second layer = .01(1-4, ∞); third layer = .05(∞). All intensity values used in these calculations were for detector configuration Θ = 60-90°, $|\Phi|$ = 0-45°. Distance separating detector pairs was 2.5 MFP.

4.0 Summary

A summary of the algorithms considered here is listed in Table 1 below.

Table 1:

Algorithm:	logI/logIo vs. R.	IogI/logIo vs. R for $\Theta_1$and Θ_2.	$(\log I_1/\log I_2)(\log I_2/\log I_1)$ref vs.R
Information obtained:	Either $\Sigma a/\Sigma t$ or Σt.	$\Sigma a/\Sigma t$ and Σt.	Depth of boundary, $\Sigma a/\Sigma t$, Σt, detection of third layer.
Necessary prior knowledge:	Σt to get $\Sigma a/\Sigma t$. or $\Sigma a/\Sigma t$ to get Σt, Io; k, slope of replot.	Io for at least two different detector orientations.	$I1_{ref}$ and $I2_{ref}$ for homogeneous media with same properties as first layer.
Application/ limitation:	Test medium must be thick, homogeneous, isotropic scattering.	Single or multilayer media; requires large lookup table.	Multilayer media. Requires calibration against reference medium.

The utility of the algorithms applied to multilayer media rely on obtaining differential responses from coupled pairs of detectors. In this regard, conditions which restrict the volume of medium that contributes significantly to a detector response (i.e. use of more tightly collimated detectors than those modeled here and the presence of anisotropic scattering) should aid in maximizing these responses.

5.0 References

1. S. Takatani and M.D. Graham. "Theoretical analysis of diffuse reflectance from a two-layer tissue model", IEEE Transactions on Biomedical Engineering, 26, pp. 656-664, 1979.
2. R.A.J. Groenhius, H.A. Ferwerda, and J.J. Ten Bosch, "Scattering and absorption of turbid materials determined from reflection measurements. 1. Theory", Applied Optics, 22, pp 2456-2462, 1983.
3. R.A.J. Groenhius, J.J. Ten Bosch, and H.A. Ferwerda, "Scattering and absorption of turbid materials determined from reflection measurements. 2. Measuring method and calibration", Applied Optics, 22, pp 2463-2467, 1983.
4. R. Nossal, J. Kiefer, G.H.Weiss, R. Bonner, H. Taitelbaum, and S. Havlin, "Photon migration in layered media", Applied Optics, 27, pp 3382-3391,1988.
5. H. Taitelbaum, S. Havlin, and G.H. Weiss, "Approximate theory of photon migration in two-layered medium", Applied Optics, 28, pp, 2245-2249,1989.
6. J.M. Schmitt, G.X. Zhou, E.C. Walker, and R.T. Wall, "Multilayer model of photon diffusion in skin" J. Opt. Soc. Am. A., 7, pp 2141-2153,1990.
7. R.L. Barbour, H. Graber. J. Lubowsky and R. Aronson, "Monte Carlo modeling of photon transport in tissue", Biophys. J., 57, pp 381a-382a, abst no.'s 599-601, 1990.
8. R.L. Barbour, H. Graber, J. Lubowsky and R. Aronson, "Model for 3-D optical imaging of tissue", in proceedings of International Union of Radio Science (URSI), Commission F, meeting of May 20-24, pp 147-148, 1990.
9. R.L. Barbour, J. Lubowsky, and H.L. Graber, "Use of reflectance spectrophotometry as a possible 3-dimensional spectroscopic imaging technique", FASEB J., 2, p a1772, 1988.
10. R. Aronson, R.L. Barbour, J. Lubowsky and H. Graber, "Application of transport theory to NIR medical imaging", in Modern Mathematical Models in Transport Theory. Berkhauser Press, 1990, in press.
11. R.L. Barbour, H. Graber, J. Lubowsky and R. Aronson, "Monte Carlo modeling of photon transport in tissue, V. Model for 3-D optical imaging of tissue", Biophys. J., 57, p 382a, abst no. 603, 1990.
12. R.L. Barbour, H. Graber, R. Aronson, and J. Lubowsky, "Model for 3-D optical imaging of tissue", in proceedings of 10th Annual International Geoscience and Remote Sensing Symposium (IGARSS), Vol II, pp 1395-1399,1990.
13. R.L. Barbour, H. Graber, R. Aronson and J. Lubowsky, "Imaging of subsurface regions of random media by remote sensing", SPIE, Vol 1431, accompanying paper in these proceedings, 1991.
14. J. R. Lamarsh, Introduction to Nuclear Reactor Theory, Chap 5, Addison-Wesely Publishing Co., NY, 1966.
15. J. Pachner, Handbook of Numerical Analysis Applications, Chap. 3, McGraw-Hill Book Co., NY, 1984.
16. R.F. Bonner, R. Nossal, S. Havlin, and G.H. Weiss, "Model for photon migration in turbid biological media", J. Opt. Soc. Am. A., 4, pp 423-432, 1987.
17. R.L. Barbour, H. Graber, J. Lubowsky and R. Aronson, "Monte Carlo modeling of photon transport in tissue, IV. Calculation of 3-D spatial contribution to detector response", Biophys. J., 57, p 382a, abst no. 602, 1990.